On the properties of NiO powders obtained by different wet chemical methods and calcination

Patricio Alastuey [1,3,‡], Daniel Pais Ospina [1,2,3,‡], David Comedi [1,2,3], Monica Tirado [1,3] and Oscar Marin-Ramirez [1,2,3,*]

1. Nanoproject – Laboratorio de Nanomateriales, Departamento de Física, Facultad de Ciencias Exactas y Tecnología, Universidad Nacional de Tucumán, Avenida Independencia 1800, CP 4000, Tucumán, Argentina
2. Laboratorio de Física del Sólido, Departamento de Física, Facultad de Ciencias Exactas y Tecnología, Universidad Nacional de Tucumán, Avenida Independencia 1800, CP 4000, Tucumán, Argentina
3. Instituto de Física del Noroeste Argentino (INFINOA), Consejo Nacional de Investigaciones Científicas y Técnicas (CONICET) y Universidad Nacional de Tucumán, Avenida Independencia 1800, CP 4000, Tucumán, Argentina

*Corresponding author: omarin@herrera.unt.edu.ar

‡ these authors have equal contributions.

Abstract

NiO powders were synthesized using coprecipitation, sol-gel, and hydrothermal synthesis methods. The powders were subjected to calcination in atmospheric air, followed by recalcination in an O2-rich atmosphere at 800 ºC for 2 hours each. Characterization techniques such as scanning electron microscopy, X-ray diffraction, energy dispersive X-ray spectroscopy, and microRaman spectroscopy were utilized. The coprecipitation and hydrothermal methods resulted in disaggregated sub-micrometric particles. The average size of particles obtained by coprecipitation method after calcination in atmospheric air and recalcination in O2-rich atmosphere was 360 ± 140 nm and 400 ± 130 nm, respectively. Regarding the particles obtained by hydrothermal method, the average size was 190 ± 50 and 220 ± 80 nm for calcined in atmospheric air and recalcined in O2-rich atmosphere, respectively. Conversely, the sol-gel method produced particle aggregates with an average size of 430 ± 150 nm after calcination in atmospheric air and 500 ± 200 nm for calcination in O2-rich atmosphere. X-ray diffraction analysis revealed that only the hydrothermal method yielded pure NiO without additional Ni-related phases, irrespective of the calcination procedure. In contrast, the coprecipitation sample exhibited a Ni2O3 phase after calcination in atmospheric air, which

This article has been accepted for publication and undergone full peer review but has not been through the copyediting, typesetting, pagination and proofreading process, which may lead to differences between this version and the Version of Record. Please cite this article as doi: 10.1111/jace.19433.

disappeared after recalcination in an O2-rich atmosphere. The sol-gel-derived sample maintained a Ni phase after both calcination processes. Analysis of the crystallite size demonstrated an increase after recalcination in an O2-rich atmosphere for the hydrothermal and sol-gel derived samples, while a decrease was observed for the coprecipitation-derived sample. Raman spectra exhibited defect-enabled first-order forbidden phonon modes that were sensitive to the synthesis route. The two magnon phonon modes also demonstrated dependency on the route, indicating variations in defect structures. Photocatalytic evaluation using methylene blue degradation in aqueous solutions indicated better performance for the powders recalcined in an O2-rich atmosphere.

Keywords: Wet Chemical Synthesis, NiO, X-ray diffraction, Raman spectroscopy, Photocatalysis, Two Magnon Phonon Modes.

1. Introduction

The use of semiconductor oxide has been increasing in recent years, and this trend is expected to continue in the coming years, covering a wide range of applications including chemical and biochemical sensing, energy harvesting and storage, optoelectronics devices, environmental remediation, among others [1–3]. In the electronic industry, the use of semiconductor oxides is almost limited to *n*-type doped semiconductors [4, 5], including mainly ZnO, In_2O_3 and SnO_2 [5]. Similarly, in other applications like environmental photocatalysis, the most widely used semiconductor oxide is TiO_2, which is also a *n*-type semiconductor [6, 7]. The limited usability of *p*-type semiconductors impose substantial constraints to practical applications of *pn* heterostructures formed by semiconductor oxides [4], leading to an increase in active research in the synthesis of *p*-type semiconductors oxides and the improvements of their properties [4, 8].

Among the wide gap semiconductor oxides, NiO stands out as an intriguing and promising material, mainly due to its electrical, optical, and magnetic properties. NiO is an intrinsic *p*-type semiconductor with a band gap energy within the range of 3.15 to 4.0 eV [9] that can be precisely controlled by adjusting the oxygen content in its crystalline lattice. In other words, the optical and

electronical related properties of NiO can be tuned in the synthesis by manipulating the experimental parameters that impact its stoichiometry.

This capability to fine adjustment of its properties renders it a multifunctional material with a variety of applications that include environmental photocatalysis, solar cells, electrochromic films, and antibacterial coatings.

Given the pressing concern of environmental remediation and particularly water purification, the development of semiconductor structures with enhanced photocatalytic properties remains an area of intense interest among the scientific community, industries, and governments worldwide. Although TiO_2-based photocatalysts have been shown to have excellent activities for the degradation of a wide list of pollutants, they have also presented some disadvantages, such as low charge carrier mobilities, photocorrosion under prolonged UV exposure and difficult catalyst recovery. For this reason, research on TiO_2 and other semiconductor oxide-based photocatalysts remains very active nowadays. Particularly, there has been a significant surge of interest in utilizing NiO as a photocatalyst for water treatment in the recent years, primarily driven by its small electron affinity (~1.7 eV). This gives it the capability to form pn junctions with various n-type semiconductor oxides [9], which in turn results in enhanced e-h recombination times and, consequently, improved photocatalytic activities. Furthermore, although NiO has an antiferromagnetic behavior, the synthesis of NiO with ferromagnetic response has been reported [10], which could facilitate the recovery of the photocatalyst material from the treated water without the need to add new components. An alternative approach to facilitate the recovery of photocatalysts used after a photocatalytic process is to use submicron sized particles instead of nanoparticles. The use of such particles will allow a simplified separation process through precipitation followed by filtration. In addition, although the nanosized photocatalysts tend to have higher photocatalytic efficiencies than microsized ones, the difficulties in nanoparticles recovery, the potential risk of leaching into the environment and the underestimated health-associated risks, have triggered interest in microparticulate systems. Therefore, part of the research efforts should focus on improving the photocatalytic efficiency of such systems. For example, it was recently reported that nanostructuration of ZnO and Cd-doped ZnO sub-microparticles results in the

enhancement of the photodegradation rate of methylene blue under UV light [11]. Also, it was reported that concave AgI sub-microparticles exhibit higher rhodamine B photodegradation rate compared to spherical AgI sub-microparticles [12].

Besides the fine-tuning of physical and chemical characteristics that have impact on photocatalytic properties, the synthesis process should also be studied to establish the relation between synthesis and properties.

In this work, the synthesis of NiO powders composed of sub-micrometric particles was investigated using three chemical wet methods: hydrothermal, coprecipitation, and sol-gel, and followed by calcination at 800 ºC under atmospheric air and recalcination at 800 ºC under O_2-rich atmosphere. The impact of each synthesis strategy on the morphological, structural, vibrational, and photocatalytic properties of the NiO powders was examined and discussed. By employing the coprecipitation and hydrothermal methods, the synthesized NiO powders exhibited disaggregated particles, in contrast to the particulate aggregate structure obtained through the sol-gel process. Furthermore, only the hydrothermal method proved successful in producing a pure NiO powder, free from any additional Ni-related phases. Analysis of the lattice parameters, microstrain and Raman spectroscopy revealed changes that indicated the presence of a high density of point defects in the growing NiO powders.

The significance of conducting a comparative analysis of these synthesis method lies in their capacity for large-scale production and the potential to obtain NiO powders on an industrial basis. Moreover, existing literature often tends to focus on individual methods, thereby neglecting a comprehensive understanding of the strengths and weaknesses associated with each method of synthesis.

2. Experimental part

Nickel Oxide powders were synthesized by three different methods: coprecipitation, hydrothermal and sol-gel, each one followed by two different calcinations: in O_2 and atmospheric air.

For coprecipitation route, 25 mL of 0.1 M aqueous solution of NaOH (J.T.Baker® ACS 98,9%, CAS number 1310-73-2) was added dropwise to 100 mL of 0.1 M aqueous solution of $NiCl_2 \cdot 6H_2O$ (Supelco EMSURE ® ACS 99%, CAS number 7791-20-0) and left stirring for 5 minutes. The solid obtained was isolated by centrifugation, washed with water 3 times and then dried at 100 ºC for 4 hours. Finally, the powder was calcinated at 800 ºC for two hours in a tubular furnace in atmospheric air. The powder was ground in an Agatha mortar for 30 minutes before and after calcination.

For hydrothermal route, 5 mL of 0.5 M aqueous solution of $NiCl_2 \cdot 6H_2O$ and 5 ml of 1.0 M aqueous solution of hexamethylenetetramine (HMTA, Panreac® ACS 99,0%, CAS number 100-97-0) were added to a 25 mL PTFE vessel, which was put on a stainless-steel autoclave. The autoclave was heated to 125 °C and held at this temperature for 16 h. Finally, the autoclave was cooled to room temperature. The solid obtained was isolated by centrifugation and the process from this point on was similar to the described for coprecipitation method.

In contrast to the two previous methods, for sol-gel ethanol (Cicarelli® ACS 99.5%, CAS number 64-17-5) was used as solvent. For this, 4.82 mL of diethanolamine (DEA, Cicarelli® ACS 98.5%, CAS number 111-42-2) was added to 100 mL of 0.1 M ethanolic solution of $NiCl_2 \cdot 6H_2O$ previously heated to 70 ºC, to obtain a 5:1 DEA:Ni^{2+} relation. The solution was maintained at 70 ºC under stirring for two hours to promote the formation of a stable colloidal phase. Then, the temperature was raised to 80 °C to increase the rate of solvent evaporation and to form a gel. The obtained gel was calcined at 300 °C for 2 hours in an oven in order to decompose the organic phase and to obtain a xerogel. Finally, it was calcinated at 800 ºC for two hours in a tubular furnace in atmospheric air. The powder was ground in an Agatha mortar for 30 minutes after calcination.

A portion of the powders obtained after calcination in atmospheric air underwent a secondary calcination process at 800 °C for two hours under a constant flow of O_2 (5 sccm) and Ar (95 sccm). The respective flowcharts of each synthesis route are shown in Fig. S1-S3 of the supplementary material.

The powders morphology was studied using scanning electron microscopy (SEM) (Carl-Zeiss Supra 55-VP). The elemental composition was determined by energy-dispersive X-ray spectroscopy (EDS). Crystalline phases and their structure were studied by X-ray diffraction (XRD) [Malvern Panalytical Empyrean diffractometer with Cu Kα radiation source (λ = 1.54056 Å)]; patterns were recorded in the 20°–90° 2θ range using an PIXcel3D area detector. MicroRaman measurements were carried out by using a 532 nm wavelength, 10 mW power laser (DXR Smart Raman Spectrometer, Thermo Scientific). Photocatalysis experiment was conducted using methylene blue (MB) as model colorant. For this purpose, a 5 mg/L of MB aqueous solution was prepared; 15 mg of NiO in 50 mL of MB solution was used as a photocatalyst. The methylene blue solution containing the NiO was illuminated during 2 h with an Ultra Vitalux 300 W E27 lamp that has an emission between 200 to 2500 nm. The degradation of colorant was measured by absorbance spectroscopy in the 200–900 nm range using a deuterium-halogen source, optical fibers and a CCD spectrometer (UV/VIS/NIR absorbance Avantes® bundle).

3. Results and Discussion

Morphologies of all obtained samples are shown in the Fig. 1(a-f) and measured sizes are summarized in the Table 1. Samples synthesized through the coprecipitation method [Fig. 1(a,b)] and by hydrothermal methods [Fig. 1(e,d)] are formed by nearly disaggregated particles. As it can be seen from the histograms shown in the Fig. 2(a-f), there was a significant dispersion in particle size for all samples. The average size of particles obtained by coprecipitation method after calcination in atmospheric air and recalcination in O_2-rich atmosphere was 360 ± 140 nm and 400 ± 130 nm, respectively. Regarding the particles obtained by hydrothermal method, the average size was 190 ± 50 and 220 ± 80 nm for calcined in atmospheric air and recalcined in O_2-rich atmosphere, respectively. Contrasting the disaggregated particle formation, the sample obtained by sol-gel [Fig. 1(e,f)] exhibited a particulate aggregate structure with average grain size of 430 ± 150 nm after calcination in atmospheric air and 500 ± 200 nm for calcination in O_2-rich atmosphere. These results show a clear and significant decrease in particle size for the hydrothermal derived powder. We find

that the particle size or grain size does not exhibit a clear trend with changes of the calcination atmosphere, and the average size values fall within the range of experimental error. Therefore, it would not be reasonable to conclusively affirm that the recalcination process has a measurable effect on the particle or grain size in our samples.

Aggregate of nanoparticles forming micro or sub-micro structures, similar to the exhibited for the sol-gel derived powder, have been reported for ZnO powders obtained through hydrothermal synthesis and for NiO powders through sol-gel where, as for the sample shown in Fig. 1(e,f), DEA was used as alkaline agent [13, 14]. It is important to remark that in alcoholic media, the reaction between DEA and metal ions can occur through the amine ligand, improving the solubility of the metallic precursor and the stability of the sol by formation of M-O-DEA chains [14, 15]. Also, the formation and precipitation of oxide or hydroxide particles is inhibited during the early stages of sol-gel process in ethanolic media using DEA as alkaline agent, until the solvent and additive evaporate during calcination, when the oxide forms. Therefore, the formation of solid particles does not take place within the liquid-phase but in a solid phase, which enables the intimate interaction between particles, hence promoting the subsequent aggregate formation.

In contrast, in both coprecipitation and hydrothermal methods, solid particles are formed in the liquid phase. In this phase, particle motion plays a crucial role in avoiding particle aggregation, thereby promoting the production of disaggregated powders. In both cases, the most probable reaction pathway involves the formation of $Ni(OH)_2$ through the reaction between Ni^{2+} and OH^- ions, the latter being provided to the reaction media by NaOH and HMTA for coprecipitation and hydrothermal methods, respectively. Subsequently, $Ni(OH)_2$ transforms into NiO upon calcination at high temperatures. Regarding the observed differences in average particle size obtained by coprecipitation and hydrothermal methods, it may be attributed to the mechanism of decomposition of the HMTA at hydrothermal conditions, which is progressive and controlled, leading to the gradual release of OH- ions into the reactive media [16, 17]. This gradual release affects the particle growth kinetics and can result in smaller particle sizes. In contrast, coprecipitation conditions involve the abrupt release of OH^- ions into the media, making them immediately available for reaction.

In Fig. 3(a,b), diffraction patterns for powders obtained by the different synthesis routes and calcination atmospheres are shown, while Fig. 3(c,d) provide a zoomed-in view of the low intensity range within these patterns, enabling a clearer observation of the secondary phases. As is clearly observed in Fig. 3(a) and 3(b), the diffraction patterns of all powders calcined in atmospheric air and oxygen atmosphere, respectively, exhibit five main reflections centered around ~37.2º, ~43.2º, ~62.8º, ~75.3º and ~79.3º. For the powder obtained by coprecipitation method and calcined in atmospheric air, additional reflections were observed around ~31.7º, ~45.3º, ~56.4º and ~66.2º, which disappear after calcination in O_2 atmosphere, as is clearly observed in Fig. 3(c,d). In the case of the powder obtained by hydrothermal method, no additional reflections were observed both in air and in O_2 calcination; while for the case of the powder obtained by sol-gel using DEA, small intensity reflections were observed around ~44.5º and ~51.8º after calcination in atmospheric air that remain observable even after calcination in O_2 atmosphere (see Fig. 3(c,d)). The diffraction patterns were compared with those reported in the literature: the five reflections centered around ~37.2º, ~43.2º, ~62.8º, ~75.3º and ~79.3º are in good agreement with the (111), (200), (220), (311) and (222) planes of face-centered cubic (*fcc*) NiO phase (space group of $Fm\bar{3}m$) [18–20]. The four reflections centered around ~31.7º, ~45.3º, ~56.4º and ~66.2º observed for sample obtained by coprecipitation method after the calcination in atmospheric air, are in good agreement with the Ni_2O_3 with hexagonal phase according to the JCPDS card number 00-014-0481. Finally, the reflections centered around ~44.5º and ~51.8º observed in the powders obtained by sol-gel corresponds to the *fcc* Ni phase [21].

As is evident, only the hydrothermal method was successful in producing a pure NiO powder without the presence of any additional Ni-related phases, regardless of the calcination procedure used; in contrast, it was observed that the Ni_2O_3 phase, which was present in the powder obtained by coprecipitation method after the calcination in atmospheric air, was eliminated upon subjecting the powder to recalcination in an O_2-rich atmosphere, leading to the formation of a pure NiO phase. In the other hand, the sol-gel synthesized powder exhibited a different behavior, in which the Ni phase observed after the calcination in atmospheric air persisted even after calcination in an O_2-rich atmosphere. This observation suggests that the Ni phase grew within the core of the NiO

microstructure, rather than at the NiO surface or grain boundaries, since oxidation to NiO would have been observed in those cases.

As for Ni_2O_3, it has been reported as an unstable oxide that can only be obtained through stabilization during the growth process on the surface of other oxides, and remains as a poorly characterized material without a full understanding of its properties [22, 23]. Despite this, the synthesis of pure Ni_2O_3 nanoparticles by the coprecipitation in NaOH and NaClO reactive media has recently been reported [24]. It is interesting to note that to obtain NiOOH, a possible precursor to obtain Ni_2O_3 by coprecipitation method, NaClO is also used to oxidize $Ni(OH)_2$ [25]. Taking the above into account, it is possible to postulate that in the presence of a highly concentrated NaOH solution and reactive chloride, the Ni^{2+} reacts to form both $Ni(OH)_2$ (with Ni oxidation state of 2+) and NiOOH (with Ni oxidation state of 3+), which may be given by a low yield parallel reaction formation of NiClO that can oxidized the Ni^{2+} to Ni^{3+}. Therefore, a possible reaction path can be hypothesized as:

$$NiCl_2 \rightleftarrows Ni^{2+} + 2Cl^- \quad (1)$$

$$NaOH + Cl^- \rightleftarrows NaClO + H^+ \quad (2)$$

$$Ni^{2+} + 2OH^- \rightleftarrows Ni(OH)_2 \quad (3)$$

$$2Ni(OH)_2 + NaClO \rightleftarrows 2NiOOH + NaCl + H_2O \quad (4)$$

So, when a $Ni(OH)_2$/NiOOH mixture is subjected to elevated temperature, NiO/Ni_2O_3 is formed. Is interesting to note that the recalcination in an oxidating condition as a the O_2-rich atmosphere, led to the disappearance of Ni_2O_3 obtaining a NiO pure phase, i. e. the Ni^{3+} was reduced to Ni^{2+}, which seems counterintuitive. However, the spontaneous Ni^{3+} reduction to Ni^{2+} mediated by lattice O^{2-} has been reported in atmospheric air [26]. A previous experiment where NiO was synthesized by coprecipitation method but calcinated in atmospheric air at 300 ºC (see Fig. S4 in the supplementary material) showed a higher concentration of Ni_2O_3 compared to that calcined at 800 ºC, so the disappearance of Ni_2O_3 in the second calcination process may not be related to the atmosphere in

which the process was carried out but to the calcination time. This indicates that the elimination of Ni_2O_3 is indeed promoted by lattice induced reactions.

To minimize experimental errors and accurately estimate the lattice parameter of the NiO phase, a Nelson-Ridley plots were made [27]. For this purpose, the lattice parameter was calculated for different planes by combining the well-known Bragg's equation $\lambda = 2dsin\theta$ with the interplanar spacing equation for the cubic system $d = a/\sqrt{h^2+k^2+l^2}$ and plotting these values in the *y*-axis against an error function $f(\theta)$ [28, 29]:

$$f(\theta) = \frac{cos^2\theta}{sin^2\theta} + \frac{cos^2\theta}{\theta} \quad (5)$$

The lattice parameter can be determined with high precision by linear regression and extrapolation of Eq. 5 to the *y*-intercept ($f(\theta) = 0$) [27], as shown in the Fig. 4(a). In Fig. 3(b) the obtained lattice parameters are presented and as can be seen, they were influenced by both the synthesis route and the calcination atmosphere, ranging between 4.1782 and 4.1788 Å. These values are higher than those reported in the literature, both experimentally, 4.1684 Å, as well as predicted by DFT calculations, 4.17 Å [30–32].

In Fig. 4(b), the following trends can be observed: (i) For the sample obtained by hydrothermal synthesis, the lattice parameter increased after the re-calcination in the O_2-rich atmosphere, contrasting with the sol-gel and coprecipitation powders, whose lattice parameter decreased; (ii) The values for hydrothermal synthesis were higher than those obtained by the two other methods; (iii) For the sol-gel route, the lattice parameter changed very slightly after the different calcination process, while it was considerably modified for the sample obtained by coprecipitation. The lattice parameter of oxides is influenced by several factors, mainly by the size and charge of the constituent ions, impurities, and internal strain [33]. As demonstrated by EDS experiments (see Fig. S5 in the supplementary material), only nickel and oxygen are presents in the studied samples, so lattice parameters should be mainly fixed by the Ni^{2+}/O^{2-} ratio and strain. Given that the observed lattice parameters for the studied samples are larger than those expected from the literature, and that the Ni^{2+} ionic radius (69 pm) is smaller than the O^{2-} ionic radius (138 pm) [34, 35], a possibility is that all the NiO

samples contain excess oxygen. The increment of lattice parameter for the hydrothermal sample after the recalcination in O_2-rich atmosphere is to be expected due to the potential incorporation of additional oxygen to the lattice. As for the significant lattice parameter decrease exhibited by the sample synthetized by coprecipitation after recalcination in O_2, it is possible that it results from a complex process associated with solid state transformations such as the elimination of the Ni_2O_3 phase initially present on the NiO particles surface.

Typically, the crystallite size and lattice microstrain can be simultaneously studied using XRD data. To achieve this, there are models that examine the effects of the crystallite size and the microstrain on the diffraction peak widths as a function of the peak position (2θ), such as the Williamson-Hall method [36–38]. This method assumes that the strain broadening in isotropic in nature, that is, it is identical in all directions of the crystal [38]. Moreover, the Williamson-Hall method considers that both the crystallite size and the microstrain contribute to the broadening of the diffraction peak independently and are additive [39]. Thus, it is represented by $\beta = \beta_{size} + \beta_{strain}$, where β is the FWHM of the diffraction peaks corrected by the instrumental broadening. To obtain the crystallite size and the microstrain using the SSP model, the following equation is used [38]:

$$\beta cos\theta = \frac{K\lambda}{D} + 4\varepsilon sin\theta \quad (6),$$

where β is the corrected FWHM for each XRD peak, K is a shape factor (usually 0.9 for cubic crystals), λ is the X-ray wavelength, D is the crystallite size and ε is the microstrain. It is possible to determine the crystallite size and strain by plotting $4sin\theta$ vs. $\beta cos\theta$ and calculating the y-intercept and the slope, respectively. The Williamson-Hall plots are presented in the Fig. 5 and the results are summarized in the table 1.

As can be seen, the data obtained by Williamson-Hall method was widely dispersed, making linear regression unsuitable for accurate microstructure data extraction. Moreover, the Fig. 5(a,b) exhibited a negative slope which means a negative microstrain according to Eq. 6. In contrast to strain, which affects the entire lattice and results in the shift of diffraction peaks, microstrain impacts only a few lattice spacings, leading to the broadening of the diffraction peaks [38, 39]. The microscopic origin of the

microstrain lies in the existence of defects in the lattice, and usually its value is related to the defect density [39], hence a negative value of microstrain is a physically meaningless result [39].

As alternative, there are other models that investigate the crystallite size and microstrain as functions of the peak profile [36, 38, 40]. Among these methods, the size-strain plot (SSP) method finds widespread use since it provides a better estimation of the crystallite size and microstrain with respect to the other methods as it assigns higher weight to low-angle reflections, where accuracy and precision are comparatively larger, as opposed to those at higher angles [38]. It models the XRD peak broadening as a result of the combined effects of crystallite size broadening (Lorentzian function) and microstrain broadening (Gaussian function) [36, 38]: $\beta = \beta_L + \beta_G$. To obtain the crystallite size and the microstrain using the SSP model, the following equation is used [36, 40, 41]:

$$(d\beta cos\theta)^2 = \frac{K\lambda}{D} d^2 \beta cos\theta + \frac{\varepsilon^2}{4} \quad (7),$$

where d is the interplanar space. It is possible to determine the crystallite size and strain by plotting $d^2\beta cos\theta$ vs. $(d\beta cos\theta)^2$ and calculating the slope and y-intercept, respectively. The SSP results are presented in the Fig. 6; the corresponding crystallite size and microstrain are summarized in the table 1. As can be seen, it becomes evident that the results obtained through the SSP method exhibit a more precise linear regression fit, as opposed to the those derived from the Williamson-Hall method. In addition, both values for the microstrain and the crystallite size are positive. In consequence, we confidently attribute a higher level of reliability and accuracy to the values obtained through the SSP method [40].

As observed, for the samples obtained through hydrothermal and coprecipitation methods, the crystallite size increased after recalcination in an O_2-rich atmosphere, whereas the sol-gel obtained sample exhibited a decrease in crystallite size. The increment of the crystallite size has been previously reported for NiO powders [41]. This phenomenon can be attributed to the absorption of oxygen in the nanocrystalline boundaries and the promotion of interface reactions, which facilitate atom diffusion and consequently lead to the enlargement of crystallites [42]. However, as mentioned above, such behavior was not observed for the powders obtained by sol-gel; instead, a decrease in

crystallite size was indicated by the results obtained by both Williamson-Hall and SSP methods. With the current data, precise understanding of the behavior behind crystallite size in this sample is not possible and further experiments are needed.

After recalcination in an O_2-rich atmosphere, all samples showed a slight decrease in microstrain values with respect to those calcined under atmospheric air. Notably, the sample obtained via sol-gel recalcination in O_2-rich atmosphere exhibited both the lowest microstrain and the lowest lattice parameter. These findings strongly suggest that this particular sample possessed a lower density of defects compared to the other samples.

To obtain more information about the behavior of defects and the vibrational properties of the studied powders, we carried out Raman experiments. In Figure 7(a,b), the Raman spectra for the powders calcined in atmospheric air (7a) and recalcined in O_2-rich atmosphere (7b) are presented. The Raman spectra were characterized by peaks centered at ~400-413, ~500, ~560-570, ~730, ~906, ~1090 and ~1450 cm^{-1}, which agree well with those reported in the literature for the NiO structure [44, 45], without any characteristic band that can be attributed to the Ni_2O_3 phase.

According to the literature, the vibration modes centered at ~400-413 cm^{-1} and ~560-570 cm^{-1} correspond to the first-order transverse-optical (TO) and longitudinal-optical (LO) phonon modes, respectively [44, 45]. Although these phonon modes are forbidden in NiO due to the inversion of symmetry in its face-centered cubic (*fcc*) crystal structure, they can be activated by a high density of defects as well as by morphological or structural effects [44, 45]. In the range between 700 and 1100 cm^{-1}, modes corresponding to the second order optical phonons 2TO, (TO1 + LO2), and 2LO, centered at ~730, ~906 and ~1090 cm^{-1}, respectively, are seen. In addition, bands centered at ~500 cm^{-1} and 1450 cm^{-1} are detected, which correspond to interaction between one-phonon and one magnon (1P+1M) excited simultaneously and to the interaction between 2 magnons (2M), respectively [44, 45].

Although the 2M interaction is difficult to be observed in an antiferromagnetic material [45], the 2M band in NiO has been widely studied and its dependences with size, temperature and defect structure, among other parameters, have been well established [46–48]. This band, which indicates the existence of

an antiferromagnetic order in NiO [48], arise from superexchange interactions between the next-nearest-neighboring Ni^{2+} ions (NNN) in the Ni^{2+}– O^{2-}–Ni^{2+} linear atomic chain [48, 49], and in nanostructures its existence is very sensitive to the presence of point defects [49]. For example, it has been recently reported that Cu^{2+} inclusion in NiO nanoparticles results in a decrease in the intensity of the 2M band [50], and for bulk NiO film it has been reported that the absence of the 2M band responds to phenomena related to a high density of point defects that interfere with the NNN superexchange interaction [51].

In our samples, there seems to be an inverse correlation between the intensity of the band due to the first-order phonon modes (~400-570 cm^{-1}) and the intensity of the 2M band: as one becomes more intense, the other is diminished. As mentioned above, the emergence of the first-order phonon modes in a cubic crystal like NiO can be explained by the existence of structural defects [44], therefore it is possible to postulate that the higher the density of defects, the smaller the 2M band due to the break of the NNN superexchange interaction. Indeed, the behavior of lattice parameter estimated by XRD experiments and the analysis of microstrain by SSP method supports this hypothesis: The sample obtained by sol-gel route, whose Raman spectrum is dominated by 2M band for both atmospheres of calcination, exhibits a lattice parameter closer to that calculated for stoichiometric NiO and the lowest microstrain value, suggesting that it had a lower density of point defects associated with excess oxygen (Ni^{2+} vacancies, interstitial oxygen, etc.), shows the lowest intensity for the band related to the first-order phonon modes. On the other hand, the samples obtained by hydrothermal route and that presented the highest lattice parameter, show an opposite behavior for these Raman bands.

Another important feature of the 2M band is its position, which has been associated with the correlation length related to the average range of the homogeneity of the crystal lattice [48]. As expected, the correlation length is responsive to the stoichiometry and defects density, among other parameters [48, 52]. The red shift of 2M band has been related to a decrease in the correlation length [48]. The aforementioned implies that a blue shift of the 2M band may be linked to an increase in the correlation length, which can also be interpreted as a reduction in the density of point defects. As is shown in Fig. 8, a blue shift of the 2M band appeared as a function of the synthesis method, more significantly for the sol-gel obtained sample as compared to that fabricated through the hydrothermal

route. This interpretation is consistent with the interpretation of the intensity of the first-order phonon modes discussed above and support the hypothesis that the sol-gel synthesis route derived in powders with lower point defect densities.

In Fig. 9, the results for photocatalytic degradation of MB using the synthesized NiO powders as photocatalysts are shown. Absorption spectra of MB at different irradiation times are presented in Fig. 9(a-f). The powders recalcined in O_2-rich atmosphere exhibited better photocatalytic activity evidenced by a more significant decrease of the absorbance of MB. Among the atmospheric air calcined powders, the sol-gel obtained powders exhibited better photocatalytic activity, while the hydrothermal obtained powders did not show activity.

To quantify the differences in the photocatalytic activity, the relative MB concentration (C/C_0) as a function of the irradiation time is depicted in the Fig. 10, together with the Ln ($C/C_{0)}$ vs. irradiation time plot (inset) to obtain the degradation rate constant [11].

According to this, for the atmospheric air calcined powders, those synthesized by sol-gel route had a k of 0.0016 min^{-1}, degrading up to ~18% of MB present in the solution after 120 minutes of irradiation, while those synthetized by coprecipitation route had k = 0.0009 min^{-1} and a corresponding percentage of degradation of ~11%.

Regarding the powders recalcined in O_2-rich atmosphere, all powders reached similar values around ~22% MB degradation after 120 minutes of irradiation. In the case of powder obtained by coprecipitation route a value of k = 0.0021 min^{-1} was obtained, while for the powder obtained by sol-gel route a k = 0.019 min^{-1} was determined. The higher k values obtained demonstrate that recalcination in O_2 improved the photocatalytic activity to degrade MB. Although these efficiencies are far from the most efficient photocatalyst, they are in the same order as other values reported for pure NiO [53–55], and represent a good starting point to research on strategies to improve the photocatalytic activity of NiO.

Since the sample obtained by sol-gel route exhibited, in comparison with the other samples, a low level of point defects, it is possible to suggest that some of the defects created during the fabrication may act as recombination centers that result in a lower density of charge available to migrate to the NiO surface and participate in the degradation process. Since the recalcination in O_2 improved the photocatalytic activity for all samples, as well as increased the 2M Raman band associated with a decrease in Ni^{2+} vacancies, it is reasonable to relate this kind of defect with our results. Indeed, it has been reported that Ni^{2+} vacancies induce a large density of charge carrier traps originated from adjacent oxygen dangling bonds, which are responsible for hole lifetime shortening [56, 57].

4. Conclusions

NiO powders were fabricated by three wet chemical methods: sol-gel, hydrothermal and coprecipitation synthesis, followed by a first calcination in atmospheric air or a second calcination in O_2-rich atmosphere. The study of their morphological, phase composition, crystallographic, microstructural parameters, vibrational, and photocatalytic properties revealed that:

1) The hydrothermal method was successful in producing a pure NiO powder without the presence of any additional Ni-related phases, regardless of the calcination procedure used.

2) A Ni_2O_3 phase was present in the powder obtained by coprecipitation method after the calcination in atmospheric air. This phase could be eliminated by the recalcination in $Ar+O_2$.

3) The sol-gel synthesized powder exhibited a Ni phase that persisted even after both calcination procedures.

4) The analysis of XRD and Raman spectroscopy showed that all samples grew with a high density of points defects, evidenced by larger than expected NiO lattice parameters and the appearance of forbidden first order phonon modes. In addition, the behavior of the two-magnon phonon modes, related to the superexchange interactions between the next-nearest-neighboring Ni^{2+} ions in the Ni^{2+}–O^{2-}–Ni^{2+} linear atomic chain and to the crystal homogeneity correlation length, also supported this conclusion.

5) The microstructural parameters were adequately estimated using Size-Strain Plot method instead of the Williamson-Hall method. Crystallite size in coprecipitation and hydrothermal-derived powders increased after recalcination in an O_2-rich atmosphere, while for sol-gel-derived powder exhibited a decrease. Microstrain and lattice parameter analysis indicate that the sol-gel sample exhibited the lowest density of defects, a conclusion supported by the Raman results.

6) The recalcination in O_2-rich atmosphere improved the photocatalytic activity of the NiO powders for the degradation of methylene blue. Although, in general, the degradation constant is lower than other typical oxide photocatalysts in the nanoscale, the results discussed here will allow to explore new strategies to improve the photocatalytic activity of NiO microstructures.

Acknowledgements

This research was supported by ANPCyT (FONCyT – BID PICT 2018-01730 and 2019-03795), SCAIT-UNT (PIUNT E637) and CONICET (PUE 08 and PIP 2021-970).

References

1. Karthikeyan C, Arunachalam P, Ramachandran K, Al-Mayouf AM, Karuppuchamy S. Recent advances in semiconductor metal oxides with enhanced methods for solar photocatalytic applications. *J Alloys Compd*. 2020;828:154281. https://doi.org/10.1016/j.jallcom.2020.154281
2. Dalapati GK, Sharma H, Guchhait A, *et al.* Tin oxide for optoelectronic, photovoltaic and energy storage devices: A review. *J Mater Chem A*. 2021;9(31):16621–16684. https://doi.org/10.1039/d1ta01291f
3. Degler D, Weimar U, Barsan N. Current Understanding of the Fundamental Mechanisms of Doped and Loaded Semiconducting Metal-Oxide-Based Gas Sensing Materials. *ACS Sensors*. 2019;4(9):2228–2249. https://doi.org/10.1021/acssensors.9b00975
4. Xiong Y, Xu D, Feng Y, Zhang G, Lin P, Chen X. P-Type 2D Semiconductors for Future Electronics. *Adv Mater*. 2023;2206939:1–34. https://doi.org/10.1002/adma.202206939
5. Lany S. Semiconducting transition metal oxides manuscript version : accepted manuscript manuscript version : accepted manuscript. *J Phys Condens Matter*. 2015;27.
6. Luong GKT, Ku Y. Selective Oxidation of Benzyl Alcohol in the Aqueous Phase by TiO2-Based Photocatalysts: A Review. *Chem Eng Technol*. 2021;44(12):2178–2190. https://doi.org/10.1002/ceat.202100321

7. Meng A, Zhang L, Cheng B, Yu J. Dual Cocatalysts in TiO2 Photocatalysis. *Adv Mater*. 2019;31(30):1–31. https://doi.org/10.1002/adma.201807660

8. Kim T, Jeong JK. Recent Progress and Perspectives of Field-Effect Transistors Based on p-Type Oxide Semiconductors. *Phys Status Solidi - Rapid Res Lett*. 2022;16(1):1–10. https://doi.org/10.1002/pssr.202100394

9. Pintor-Monroy MI, Murillo-Borjas BL, Catalano M, Quevedo-Lopez MA. Controlling Carrier Type and Concentration in NiO Films to Enable in Situ PN Homojunctions. *ACS Appl Mater Interfaces*. 2019;11(30):27048–27056. https://doi.org/10.1021/acsami.9b04380

10. Abbas H, Nadeem K, Hassan A, Rahman S, Krenn H. Enhanced photocatalytic Activity of Ferromagnetic Fe-doped NiO nanoparticles. *Optik (Stuttg)*. 2020;202(August 2019):1–8. https://doi.org/10.1016/j.ijleo.2019.163637

11. Franco M, Marin O, Vega NC, Tirado M, Tereschuk ML, Comedi D. Surface nanostructuration of ZnO and ZnO:Cd sub-microstructures and their use as suspended and immobilized photocatalysts for rapid degradation of methylene blue. *Mater Lett*. 2022;311(December 2021). https://doi.org/10.1016/j.matlet.2021.131634

12. An C, Liu J, Wang S, *et al.* Concaving AgI sub-microparticles for enhanced photocatalysis. *Nano Energy*. 2014;9:204–211. https://doi.org/10.1016/j.nanoen.2014.07.015

13. Tangcharoen T, Klysubun W, Kongmark C. Synthesis of nanocrystalline NiO/ZnO heterostructured composite powders by sol-gel auto combustion method and their characterizations. *J Mol Struct*. 2018;1156:524–533. https://doi.org/10.1016/j.molstruc.2017.12.019

14. González V, Marin O, Tirado M, Comedi D. Metastability effects on the photoluminescence of ZnO nano-micro structures grown at low temperature and influence of the precursors on their morphology and structure. *Mater Res Express*. 2018;5(12):125003. https://doi.org/10.1088/2053-1591/aadfc4

15. Hosseini Vajargah P, Abdizadeh H, Ebrahimifard R, Golobostanfard MR. Sol-gel derived ZnO thin films: Effect of amino-additives. *Appl Surf Sci*. 2013;285(PARTB):732–743. https://doi.org/10.1016/j.apsusc.2013.08.118

16. McPeak KM, Le TP, Britton NG, Nickolov ZS, Elabd YA, Baxter JB. Chemical Bath Deposition of ZnO Nanowires at Near-Neutral pH Conditions without Hexamethylenetetramine (HMTA): Understanding the Role of HMTA in ZnO Nanowire Growth. *Langmuir*. 2011;27(7):3672–3677. https://doi.org/10.1021/la105147u

17. Marin O, González V, Tirado M, Comedi D. Effects of methanol on morphology and photoluminescence in solvothermal grown ZnO powders and ZnO on Si. *Mater Lett*. 2019;251C:41–44. https://doi.org/10.1016/j.matlet.2019.05.033

18. Kuwa M, Harada M, Sato R, Teranishi T. Ligand-Stabilized CoO and NiO Nanoparticles for Spintronic Devices with Antiferromagnetic Insulators. *ACS Appl Nano Mater*. 2020;3(3):2745–2755. https://doi.org/10.1021/acsanm.0c00092

19. Varunkumar K, Hussain R, Hegde G, Ethiraj AS. Effect of calcination temperature on Cu

doped NiO nanoparticles prepared via wet-chemical method: Structural, optical and morphological studies. *Mater Sci Semicond Process*. 2017;66:149–156. https://doi.org/10.1016/j.mssp.2017.04.009

20. Mamat MH, Parimon N, Ismail AS, *et al.* Synthesis, structural and optical properties of mesostructured, X-doped NiO (x = Zn, Sn, Fe) nanoflake network films. *Mater Res Bull*. 2020;127(March). https://doi.org/10.1016/j.materresbull.2020.110860

21. Ahghari MR, Soltaninejad V, Maleki A. Synthesis of nickel nanoparticles by a green and convenient method as a magnetic mirror with antibacterial activities. *Sci Rep*. 2020;10(1):1–10. https://doi.org/10.1038/s41598-020-69679-4

22. Ciola Amoresi RA, Cristina de Oliveira R, Cichetto L, *et al.* Pure and Ni2O3-decorated CeO2 nanoparticles applied as CO gas sensor: Experimental and theoretical insights. *Ceram Int*. 2022;48(10):14014–14025. https://doi.org/10.1016/j.ceramint.2022.01.286

23. Jouini K, Raouafi A, Dridi W, *et al.* Investigation of gamma-ray irradiation induced phase change from NiO to Ni2O3 for enhancing photocatalytic performance. *Optik (Stuttg)*. 2019;195(May 2019). https://doi.org/10.1016/j.ijleo.2019.163109

24. Dey S, Bhattacharjee S, Chaudhuri MG, Bose RS, Halder S, Ghosh CK. Synthesis of pure nickel(iii) oxide nanoparticles at room temperature for Cr(vi) ion removal. *RSC Adv*. 2015;5(67):54717–54726. https://doi.org/10.1039/c5ra05810d

25. Pan J, Du J, Sun Y, Wan P, Liu X, Yang Y. The change of structure and electrochemical property in the synthesis process of spherical NiOOH. *Electrochim Acta*. 2009;54(14):3812–3818. https://doi.org/10.1016/j.electacta.2009.01.083

26. Liu HS, Zhang ZR, Gong ZL, Yang Y. Origin of deterioration for LiNiO2 cathode material during storage in air. *Electrochem Solid-State Lett*. 2004;7(7):190–193. https://doi.org/10.1149/1.1738471

27. Suryanarayana, C., Grant Norton M. X-Ray Diffraction A practical Approach. Springer Science+Business Media New York; 1998 https://doi.org/10.1007/978-1-4899-0148-4

28. Shunmuga Sundaram P, Sangeetha T, Rajakarthihan S, Vijayalaksmi R, Elangovan A, Arivazhagan G. XRD structural studies on cobalt doped zinc oxide nanoparticles synthesized by coprecipitation method: Williamson-Hall and size-strain plot approaches. *Phys B Condens Matter*. 2020;595(April):412342. https://doi.org/10.1016/j.physb.2020.412342

29. Tigau N, Ciupina V, Prodan G, Rusu GI, Vasile E. Structural characterization of polycrystalline Sb2O3 thin films prepared by thermal vacuum evaporation technique. *J Cryst Growth*. 2004;269(2–4):392–400. https://doi.org/10.1016/j.jcrysgro.2004.05.052

30. Cairns RW, Ott E. X-Ray Studies of the System Nickel-Oxygen-Water . *J Am Chem Soc*. 1933;55:527–533. https://doi.org/10.1021/ja01329a013

31. Assefi M, Maroufi S, Yamauchi Y, Sahajwalla V. Core-Shell Nanocatalysts of Co3O4 and NiO Shells from New (Discarded) Resources: Sustainable Recovery of Cobalt and Nickel from Spent Lithium-Ion Batteries, Ni-Cd Batteries, and LCD Panel. *ACS Sustain Chem Eng*. 2019;7(23):19005–19014. https://doi.org/10.1021/acssuschemeng.9b04618

32. Walls B, Mazilkin AA, Mukhamedov BO, *et al.* Nanodomain structure of single crystalline nickel oxide. *Sci Rep*. 2021;11(1):1–10. https://doi.org/10.1038/s41598-021-82070-1

33. Zhang Y, Xu X. Modeling of lattice parameters of cubic perovskite oxides and halides. *Heliyon*. 2021;7(7):e07601. https://doi.org/10.1016/j.heliyon.2021.e07601

34. Breviglieri ST, Cavalheiro ÉTG, Chierice GO. Correlation between ionic radius and thermal decomposition of Fe (II), Co (II), Ni (II), Cu (II) and Zn (II) diethanoldithiocarbamates. *Thermochim Acta*. 2000;356:79–84.

35. Kato M, Konashi K. Lattice parameters of (U, Pu, Am, Np)O2-x. *J Nucl Mater*. 2009;385(1):117–121. https://doi.org/10.1016/j.jnucmat.2008.09.037

36. Nath D, Singh F, Das R. X-ray diffraction analysis by Williamson-Hall, Halder-Wagner and size-strain plot methods of CdSe nanoparticles- a comparative study. *Mater Chem Phys*. 2020;239(August 2019). https://doi.org/10.1016/j.matchemphys.2019.122021

37. Akl AA, Mahmoud SA, AL-Shomar SM, Hassanien AS. Improving microstructural properties and minimizing crystal imperfections of nanocrystalline Cu2O thin films of different solution molarities for solar cell applications. *Mater Sci Semicond Process*. 2018;74(November 2017):183–192. https://doi.org/10.1016/j.mssp.2017.10.007

38. Dolabella S, Borzì A, Dommann A, Neels A. Lattice Strain and Defects Analysis in Nanostructured Semiconductor Materials and Devices by High-Resolution X-Ray Diffraction: Theoretical and Practical Aspects. *Small Methods*. 2022;6(2). https://doi.org/10.1002/smtd.202100932

39. Maniammal K, Madhu G, Biju V. X-ray diffraction line profile analysis of nanostructured nickel oxide: Shape factor and convolution of crystallite size and microstrain contributions. *Phys E Low-Dimensional Syst Nanostructures*. 2017;85:214–222. https://doi.org/10.1016/j.physe.2016.08.035

40. Basak M, Rahman L, Ahmed F, Biswas B, Sharmin N. Precipitating Agent Approach. *J Alloys Compd*. 2022;895:162694. https://doi.org/https://doi.org/10.1016/j.jallcom.2021.162694

41. Jafari A, Pilban Jahromi S, Boustani K, Goh BT, Huang NM. Evolution of structural and magnetic properties of nickel oxide nanoparticles: Influence of annealing ambient and temperature. *J Magn Magn Mater*. 2019;469(March 2018):383–390. https://doi.org/10.1016/j.jmmm.2018.08.005

42. Wolfman M, Wang X, Garcia JC, *et al.* The Importance of Surface Oxygen for Lithiation and Morphology Evolution during Calcination of High-Nickel NMC Cathodes. *Adv Energy Mater*. 2022;12(16):1–12. https://doi.org/10.1002/aenm.202102951

43. Wang WN, Widiyastuti W, Ogi T, Lenggoro IW, Okuyama K. Correlations between crystallite/particle size and photoluminescence properties of submicrometer phosphors. *Chem Mater*. 2007;19(7):1723–1730. https://doi.org/10.1021/cm062887p

44. Bala N, Singh HK, Verma S, Rath S. Magnetic-order induced effects in nanocrystalline NiO probed by Raman spectroscopy. *Phys Rev B*. 2020;102(2):1–7. https://doi.org/10.1103/PhysRevB.102.024423

45. Qiu J, Nguyen TH, Kim S, *et al.* Two-dimensional correlation spectroscopy analysis of Raman spectra of NiO nanoparticles. *Spectrochim Acta - Part A Mol Biomol Spectrosc*. 2022;280(March):121498. https://doi.org/10.1016/j.saa.2022.121498

46. Gandhi AC, Huang CY, Yang CC, *et al.* Growth mechanism and magnon excitation in NiO Nanowalls. *Nanoscale Res Lett*. 2011;6:1–14. https://doi.org/10.1186/1556-276X-6-485

47. Sunny A, Balasubramanian K. Laser-induced phonon and magnon properties of NiO nanoparticles: A Raman study. *J Raman Spectrosc*. 2021;52(4):833–842. https://doi.org/10.1002/jrs.6067

48. Sunny A, Balasubramanian K. Raman Spectral Probe on Size-Dependent Surface Optical Phonon Modes and Magnon Properties of NiO Nanoparticles. *J Phys Chem C*. 2020;124(23):12636–12644. https://doi.org/10.1021/acs.jpcc.0c02638

49. Gandhi AC, Pant J, Pandit SD, *et al.* Short-Range magnon excitation in NiO nanoparticles. *J Phys Chem C*. 2013;117(36):18666–18674. https://doi.org/10.1021/jp4029479

50. Sunny A, Balasubramanian K. Phonon, magnon and magnetic properties of Cu-doped NiO nanostructures. *J Raman Spectrosc*. 2022;53(7):1249–1258. https://doi.org/10.1002/jrs.6354

51. Meng X, Du Y, Gao X. Face–centered cubic p–type NiO films room–temperature prepared via direct-current reactive magnetron sputtering–Influence of sputtering power on microstructure, optical and electrical behaviors. *Phys B Condens Matter*. 2020;579(November 2019):411897. https://doi.org/10.1016/j.physb.2019.411897

52. Menon PS, Kunjumon J, Bansal M, *et al.* Role of surface defects in the third order nonlinear optical properties of pristine NiO and Cr doped NiO nanostructures. *Ceram Int*. 2023;49(4):5815–5827. https://doi.org/10.1016/j.ceramint.2022.10.301

53. Sumantha HS, Rajagopal S, Nagaraju G, Shashank M, Suresha BL. Facile and eco-friendly combustion synthesis of NiO particles for photodegradation studies. *Chem Phys Lett*. 2021;779(June):138837. https://doi.org/10.1016/j.cplett.2021.138837

54. Wan X, Yuan M, Tie SL, Lan S. Effects of catalyst characters on the photocatalytic activity and process of NiO nanoparticles in the degradation of methylene blue. *Appl Surf Sci*. 2013;277(3):40–46. https://doi.org/10.1016/j.apsusc.2013.03.126

55. Gnanasekaran L, Hemamalini R, Saravanan R, *et al.* Synthesis and characterization of metal oxides (CeO2, CuO, NiO, Mn3O4, SnO2 and ZnO) nanoparticles as photo catalysts for degradation of textile dyes. *J Photochem Photobiol B Biol*. 2017;173(May):43–49. https://doi.org/10.1016/j.jphotobiol.2017.05.027

56. Flynn CJ, McCullough SM, Li L, Donley CL, Kanai Y, Cahoon JF. Passivation of nickel vacancy defects in nickel oxide solar cells by targeted atomic deposition of boron. *J Phys Chem C*. 2016;120(30):16568–16576. https://doi.org/10.1021/acs.jpcc.6b06593

57. Flynn CJ, McCullough SM, Oh E, *et al.* Site-Selective Passivation of Defects in NiO Solar Photocathodes by Targeted Atomic Deposition. *ACS Appl Mater Interfaces*. 2016;8(7):4754–4761. https://doi.org/10.1021/acsami.6b01090

Table 1. Structural parameters for all samples obtained from the XRD data.

Sample	Lattice param. (Å)	Williamson-Hall method		SSP method	
		Size (nm)	microtrain (ε)	Size (nm)	Microstrain (ε)
Coprecipitation – air calcined	4.1786	60.3	-5.35×10^{-6}	65.4	2.01×10^{-3}
Coprecipitation – O_2 recalcined	4.1783	83.0	1.24×10^{-4}	77.9	1.67×10^{-3}
Hydrothermal – air calcined	4.1787	51.4	-1.74×10^{-4}	58.8	1.79×10^{-3}
Hydrothermal – O_2 recalcined	4.1788	83.0	1.52 x 10-4	72.9	1.13×10^{-3}
Sol gel – air calcined	4.1782(5)	83.5	1.49×10^{-4}	77.0	1.71×10^{-3}
Sol gel – O_2 recalcined	4.1782(1)	77.0	8.96×10^{-5}	70.7	6.36×10^{-4}

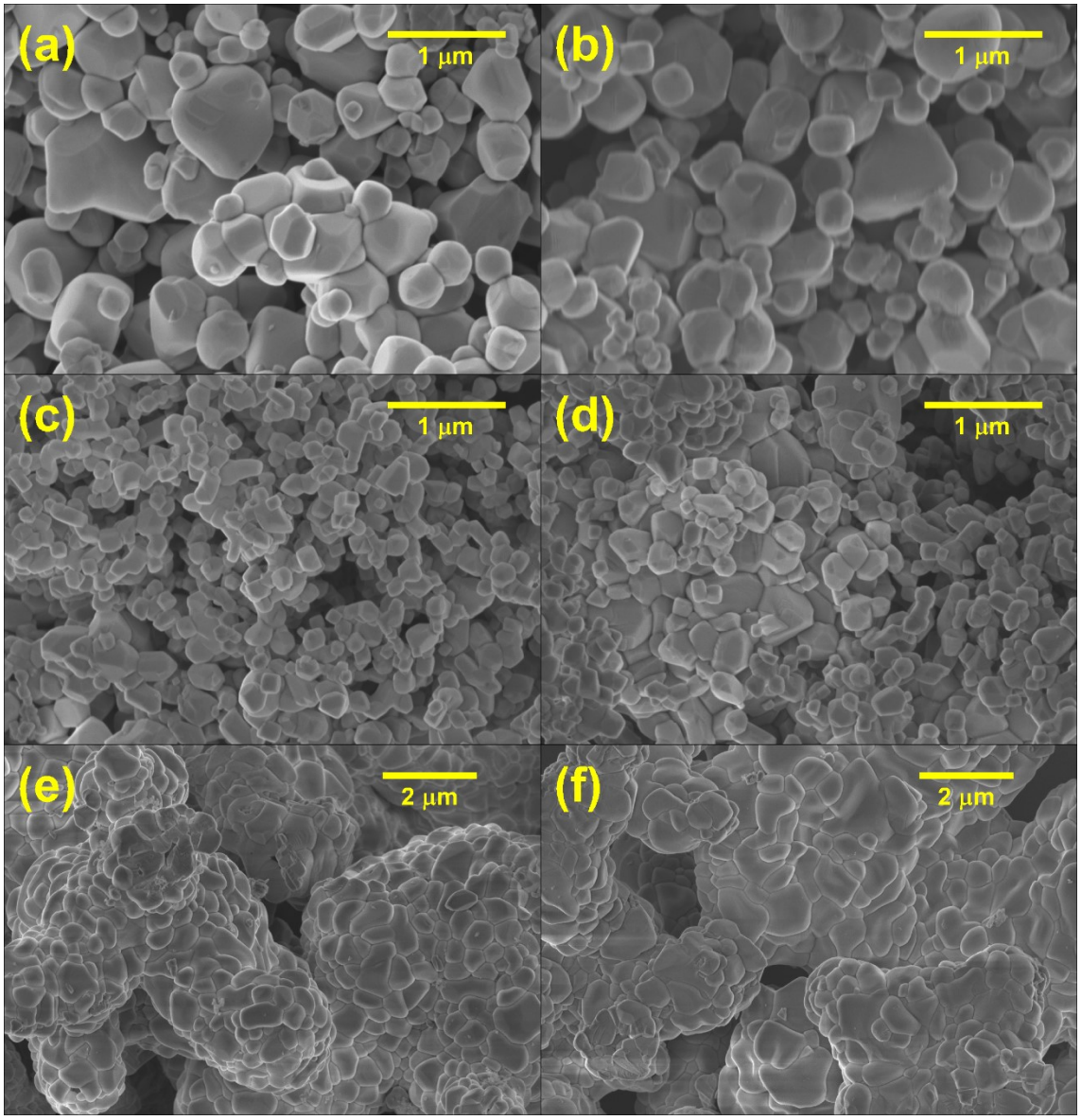

Figure 1.SEM micrographs of NiO powders obtained by; (a,b) coprecipitation and annealed in air and air followed by O_2, respectively; (c,d) hydrothermal synthesis and annealed in air and air followed by O_2, respectively; (e,f) sol-gel and annealed in air and air followed by O_2, respectively.

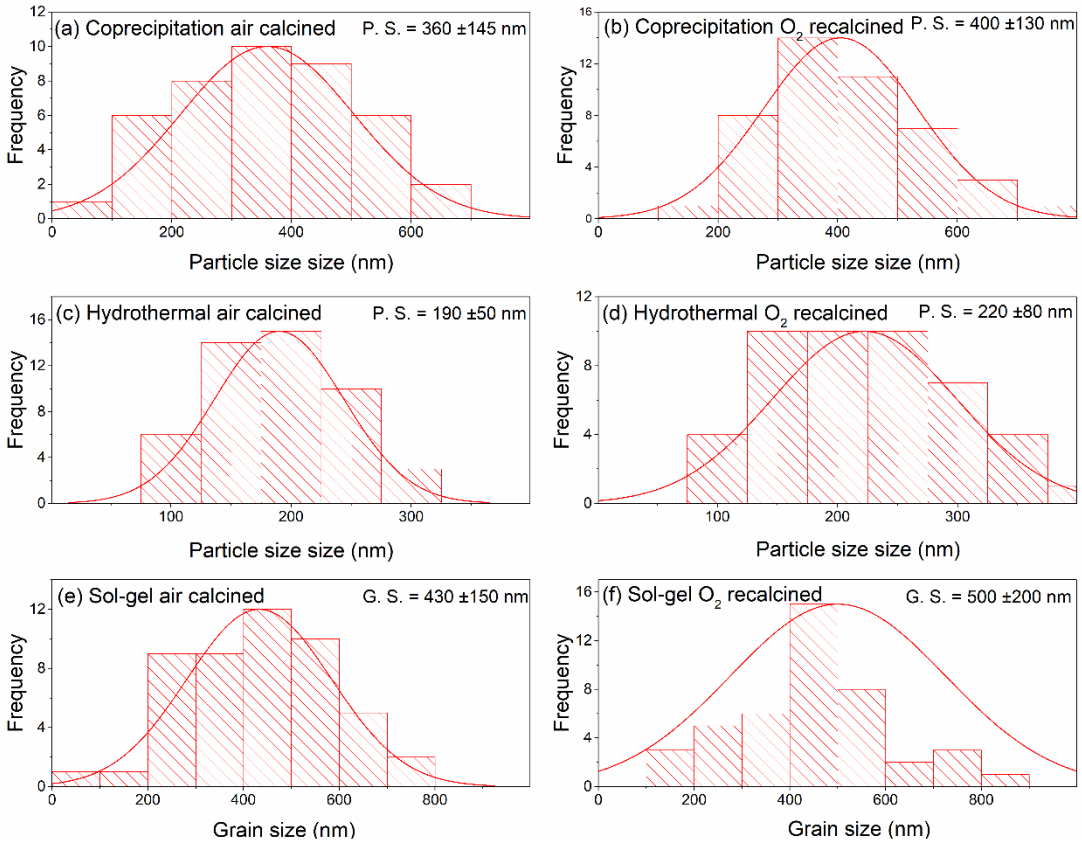

Figure 2. . Histograms of particle size (a - d) and grain size (e, f) of samples synthetized by co-precipitation (a, b), hydrothermal (c, d) and sol-gel (e, f).

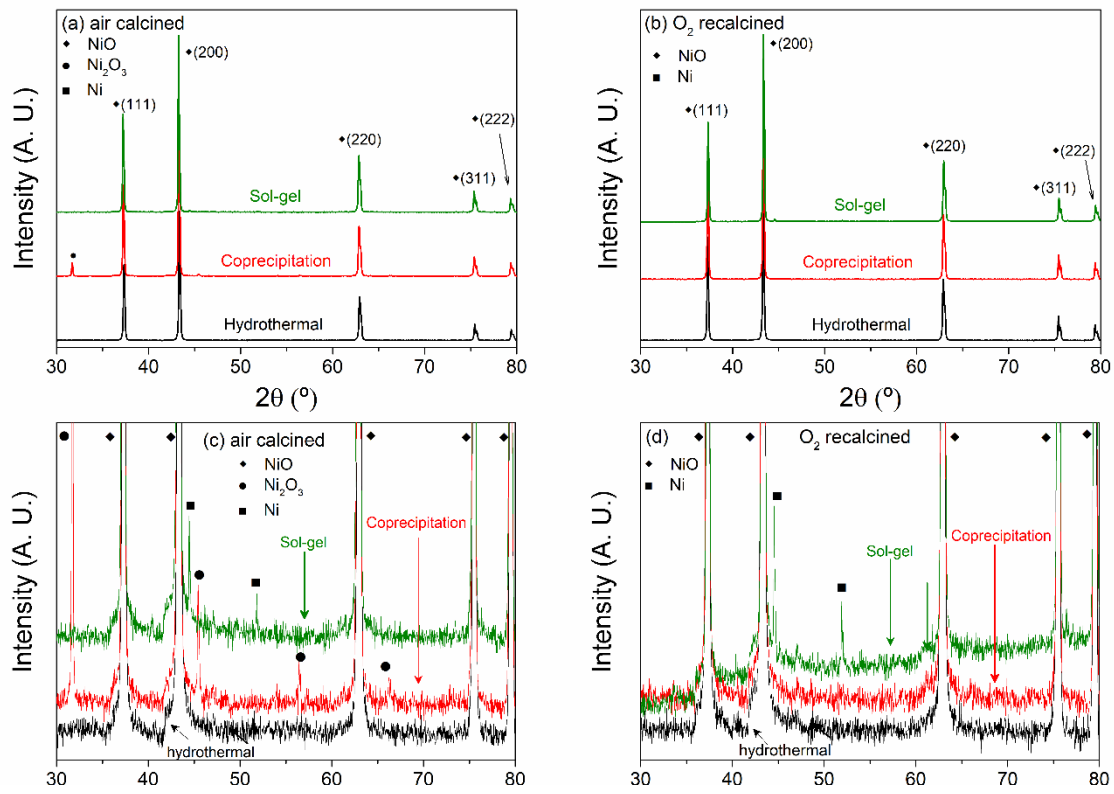

Figure 3. XRD patterns for NiO powders synthetized by sol-gel, coprecipitation and hydrothermal methods and then calcined in (a) atmospheric air, (b) after a recalcination in O_2-rich atmosphere, (c) a zoomed-in view of the low intensity range for XRD patterns for samples calcined in atmospheric air, (d) a zoomed-in view of the low intensity range for XRD patterns for samples recalcined in atmospheric in O_2-rich atmosphere.

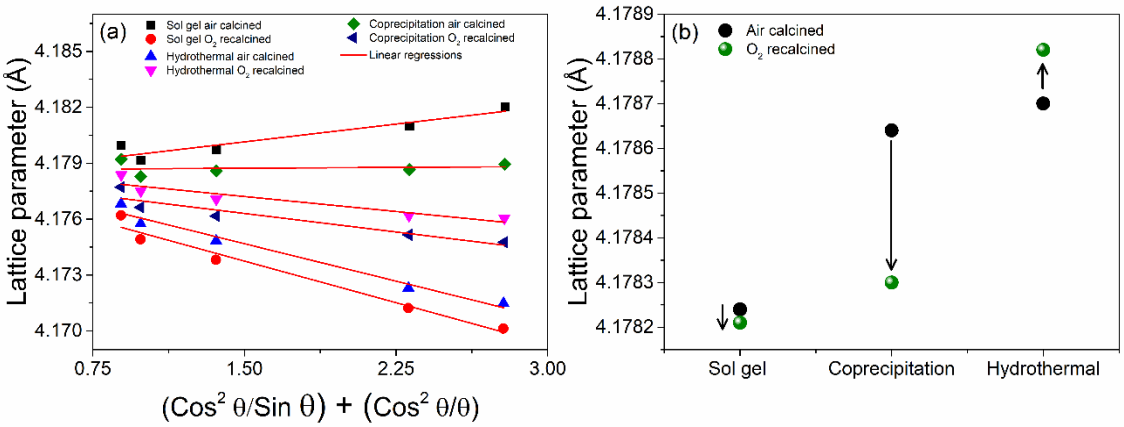

Figure 4. (a) Nelson-Ridley plots and (b) lattice parameter of NiO phase determined from XRD patterns for powders fabricated by sol-gel, coprecipitation and hydrothermal synthesis and calcined in air and in Ar+O_2.

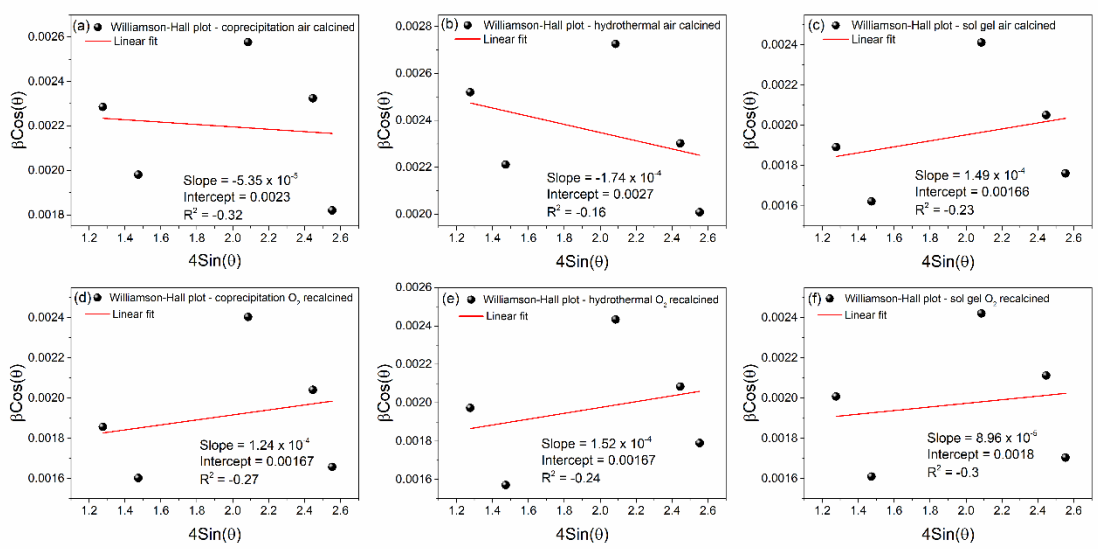

Figure 5. Williamson-Hall plot from XRD data; (a,b,c) NiO powders obtained by coprecipitation, hydrothermal and sol-gel calcined in atmospheric air, respectively; (d,e,f) NiO powders obtained by coprecipitation, hydrothermal and sol-gel recalcined in O_2-rich atmosphere.

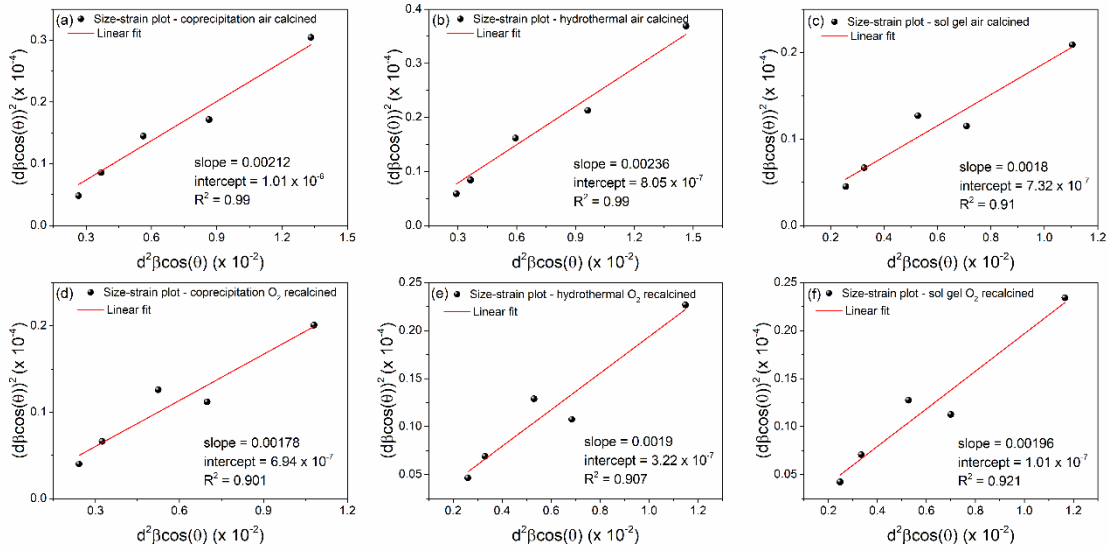

Figure 6. Size-strain plot from XRD data; (a,b,c) NiO powders obtained by coprecipitation, hydrothermal and sol-gel calcined in atmospheric air, respectively; (d,e,f) NiO powders obtained by coprecipitation, hydrothermal and sol-gel recalcined in O_2-rich atmosphere.

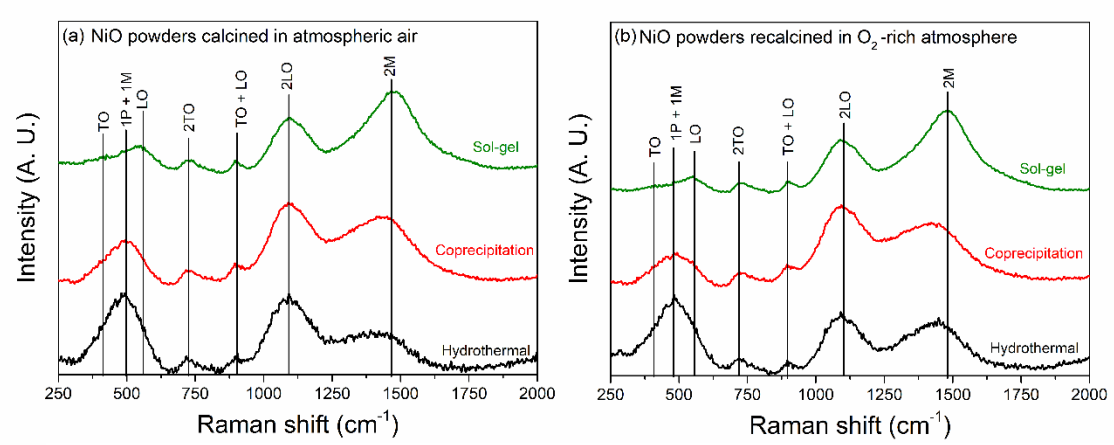

Figure 7. Raman spectra of powder samples fabricated by the different synthesis methods and calcination atmospheres. (a) Powders calcined in air; (b) Powders recalcined in O_2-rich atmosphere.

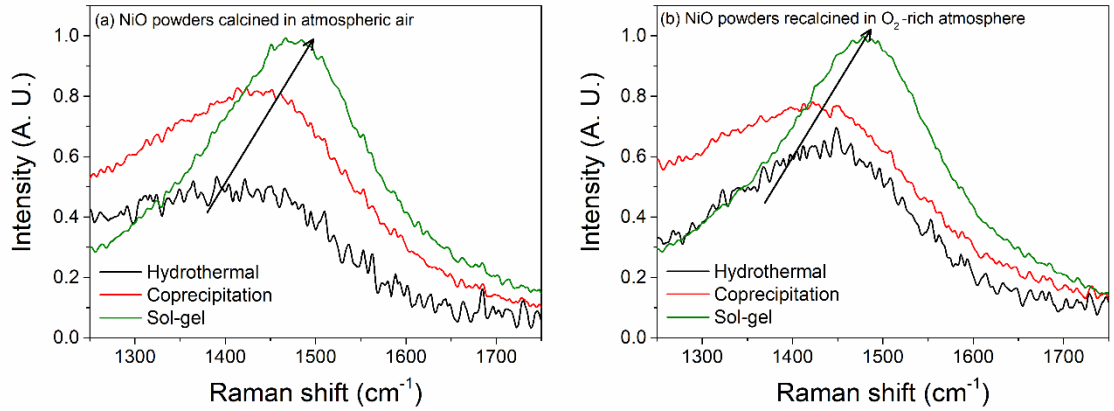

Figure 8. The Raman 2M band for the different samples, showing a blue shift for the sol-gel sample. a) Powders calcined in atmospheric air; b) Powders calcined in O_2-rich atmosphere.

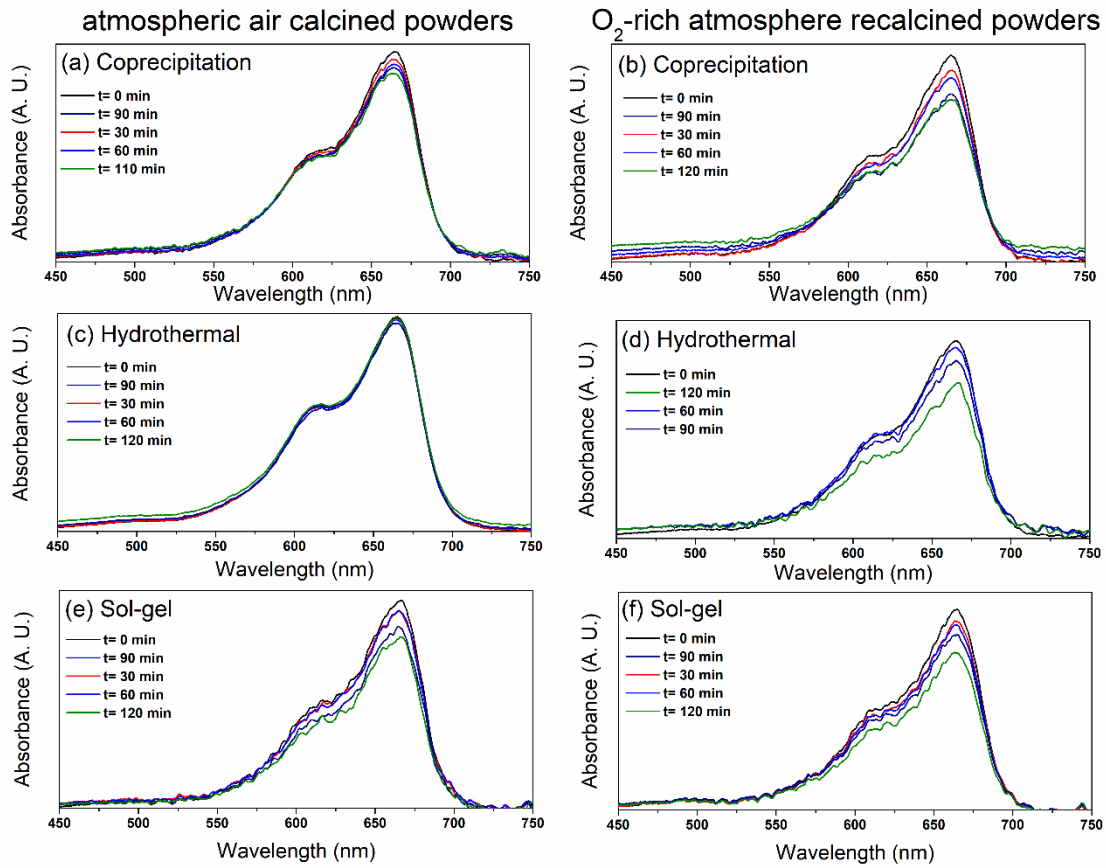

Figure 9. (a-f) Absorption spectra of MB in aqueous solutions after different times of photocatalytical degradation by the different studied powders.

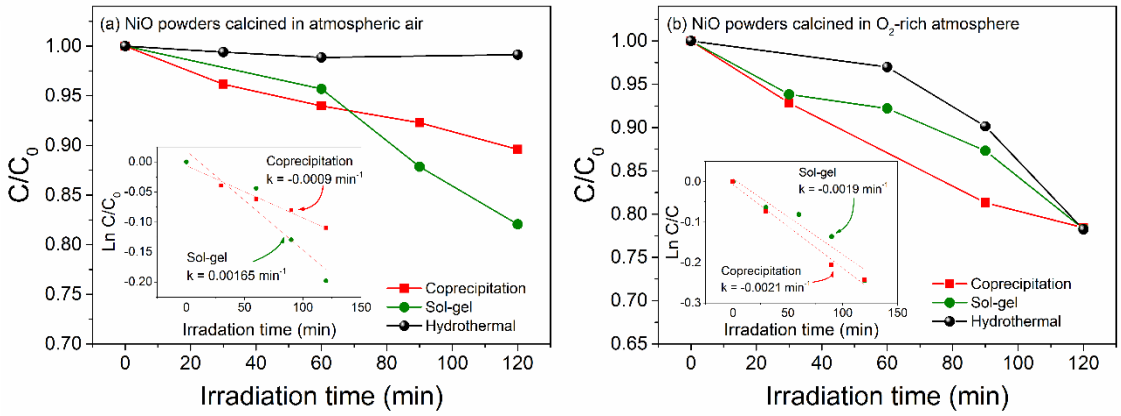

Figure 10. Relative variation of the MB concentration (C/C_0) in aqueous solution as a function of the photocatalytical degradation by powders fabricated by different synthesis routes and calcined in (a) atmospheric air and (b) in O_2-rich atmosphere. Insets: Ln C/C_0.

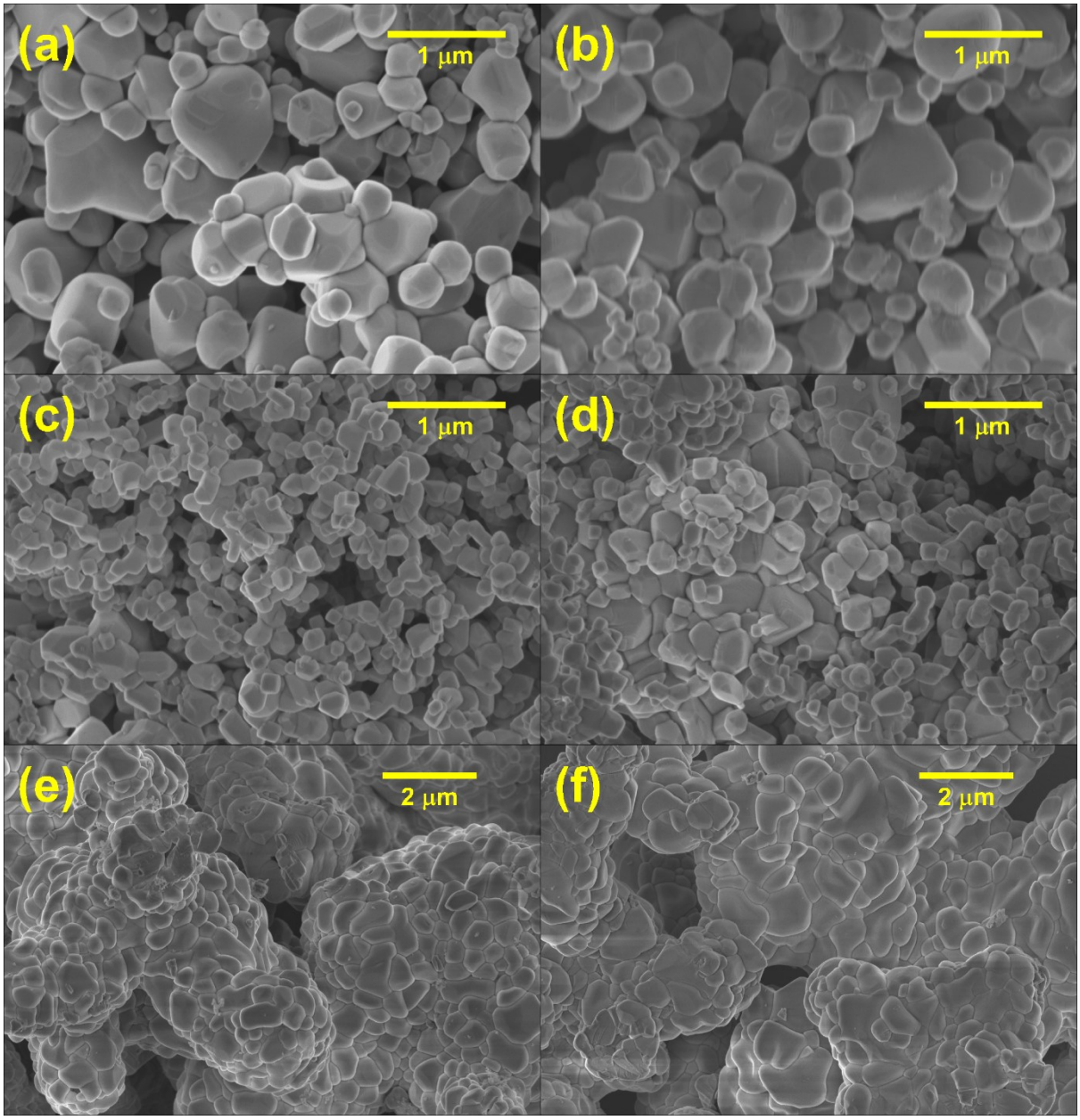

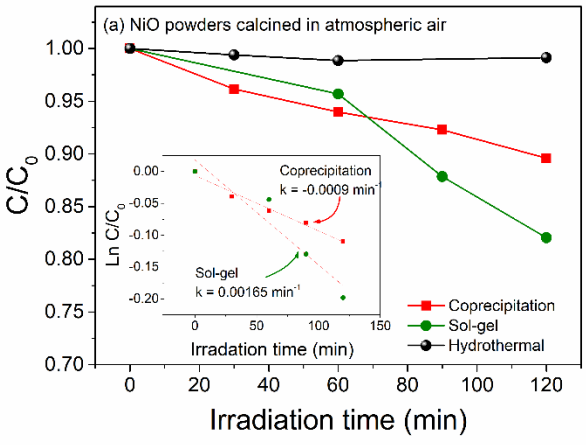

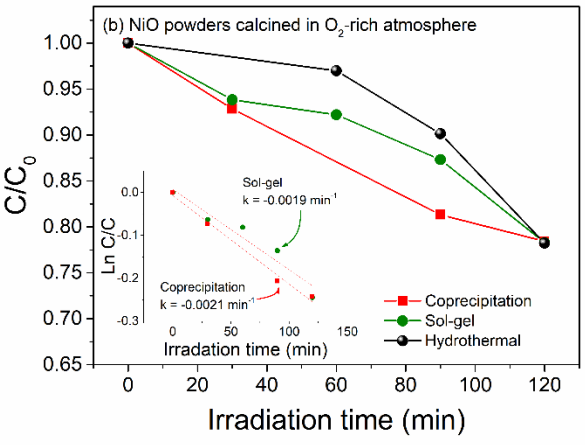

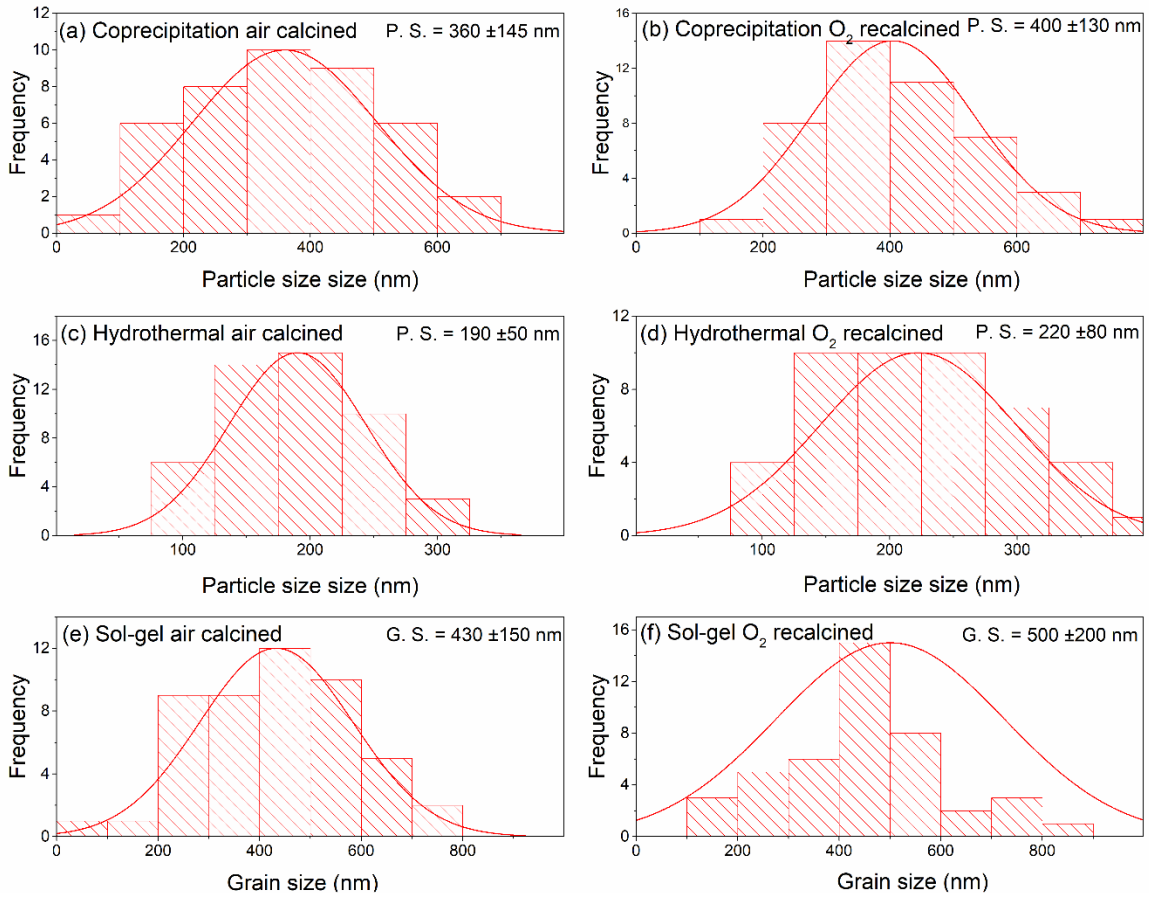

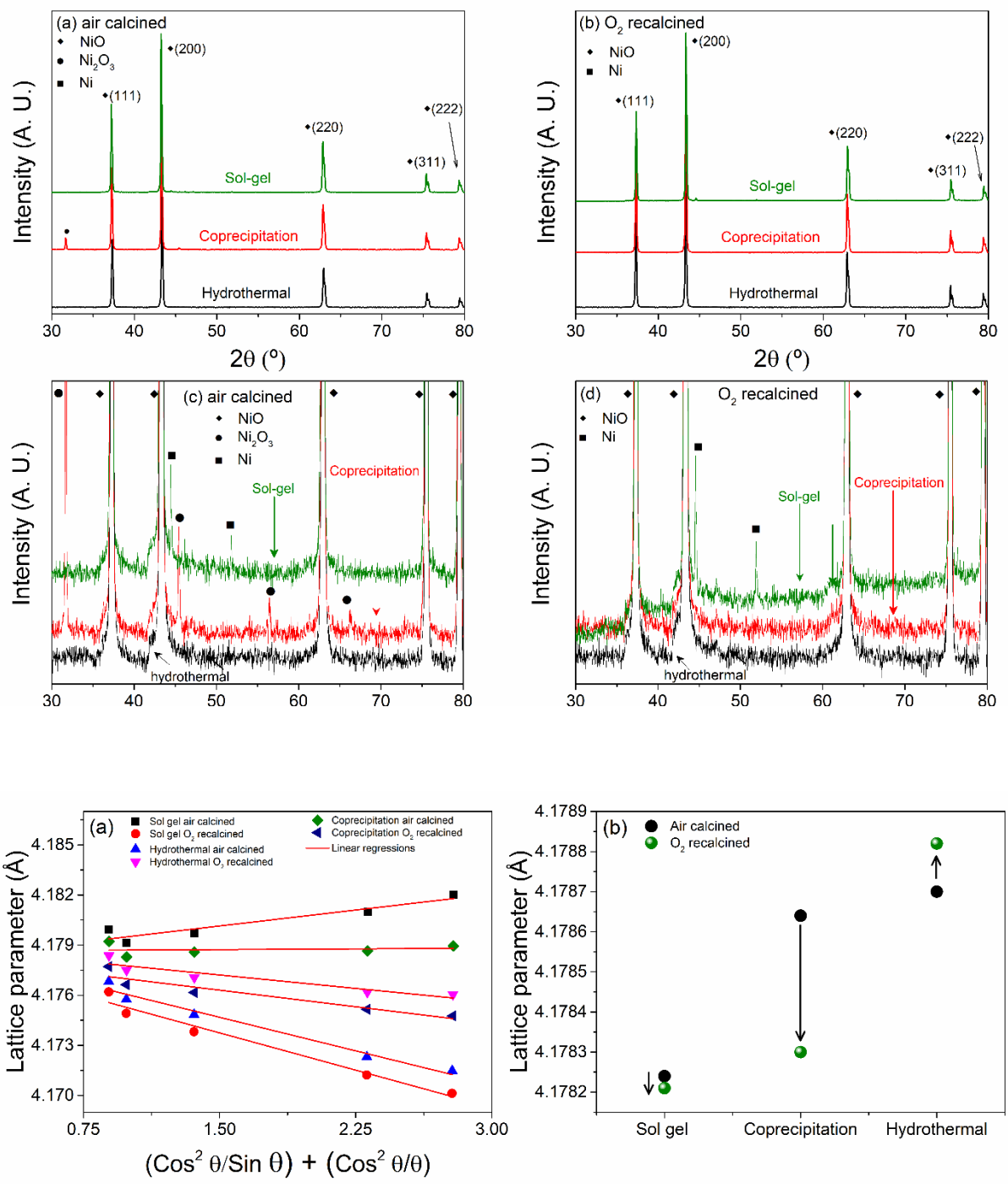

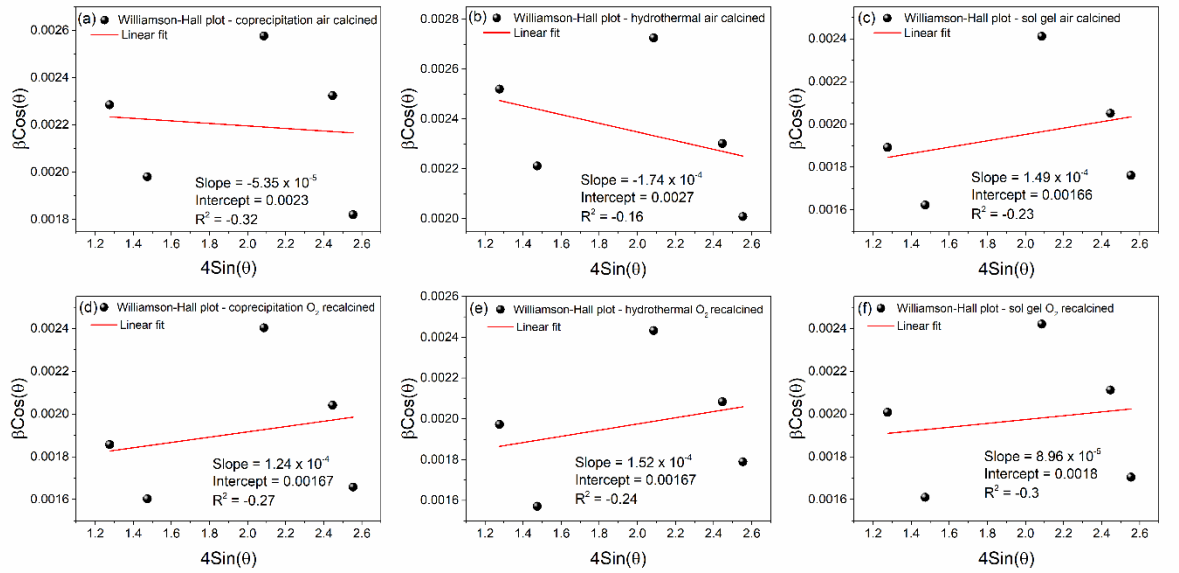

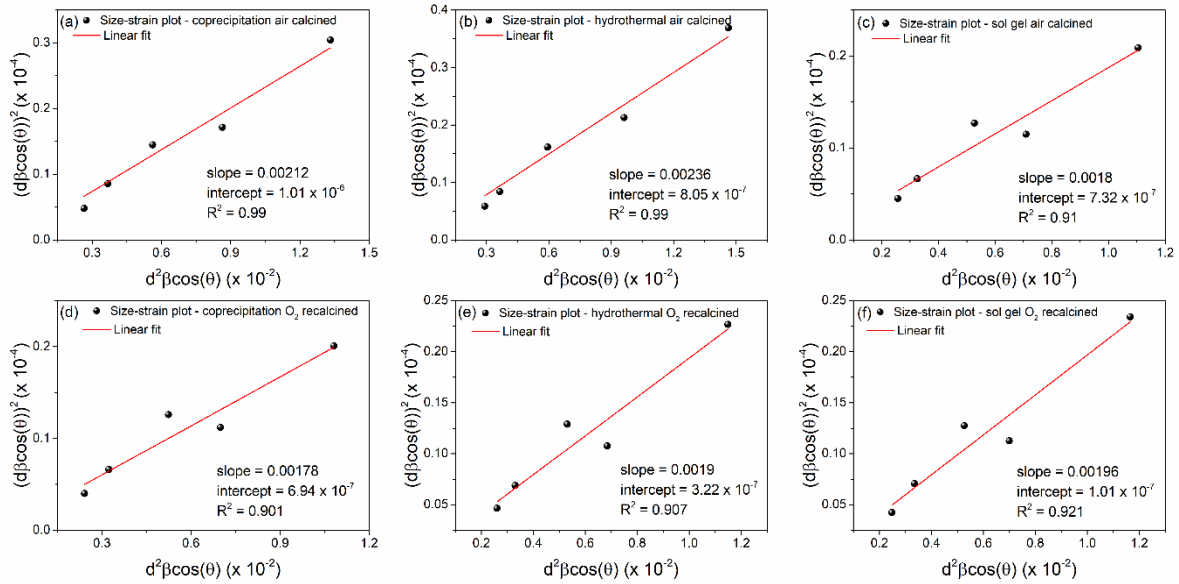

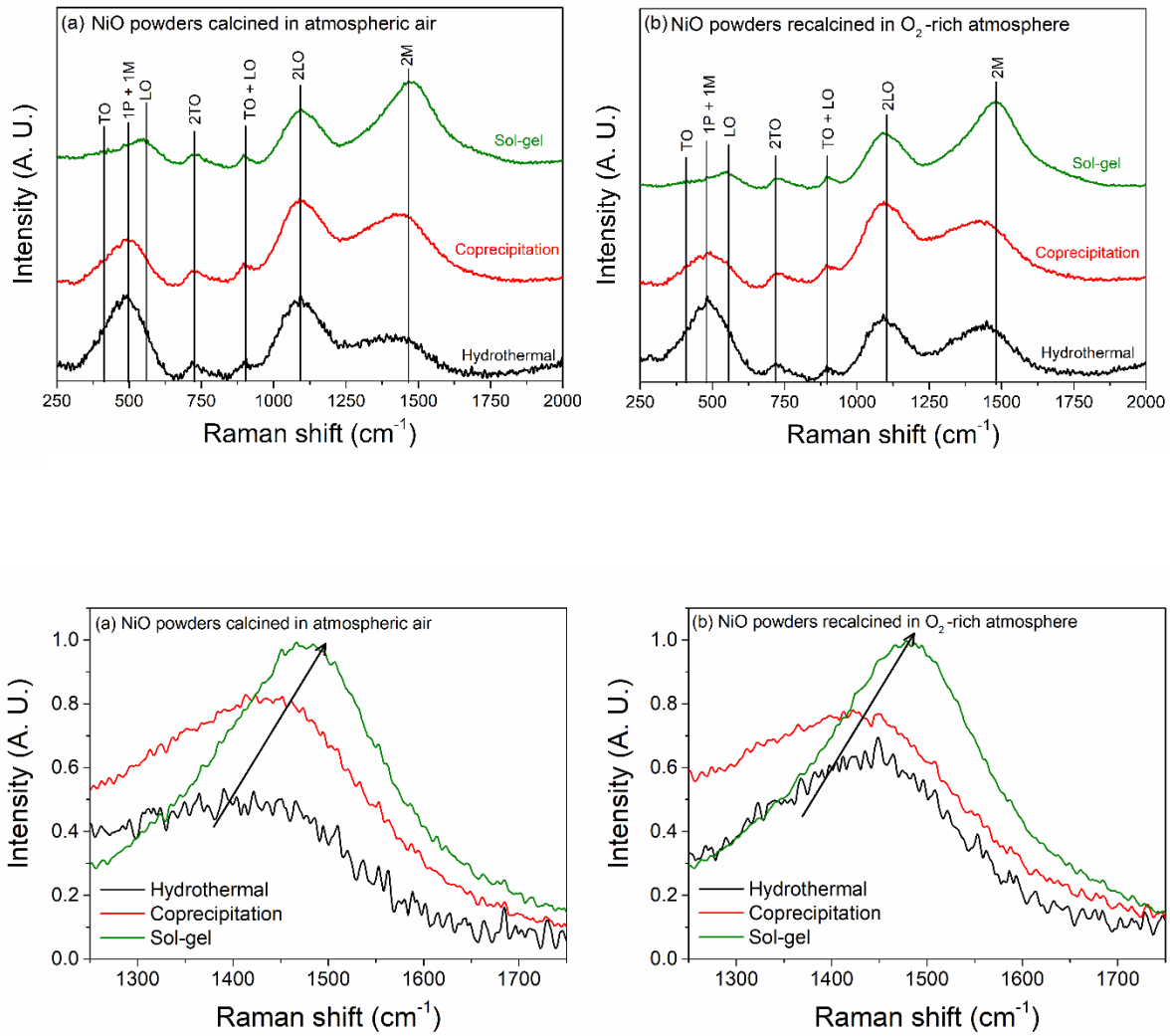

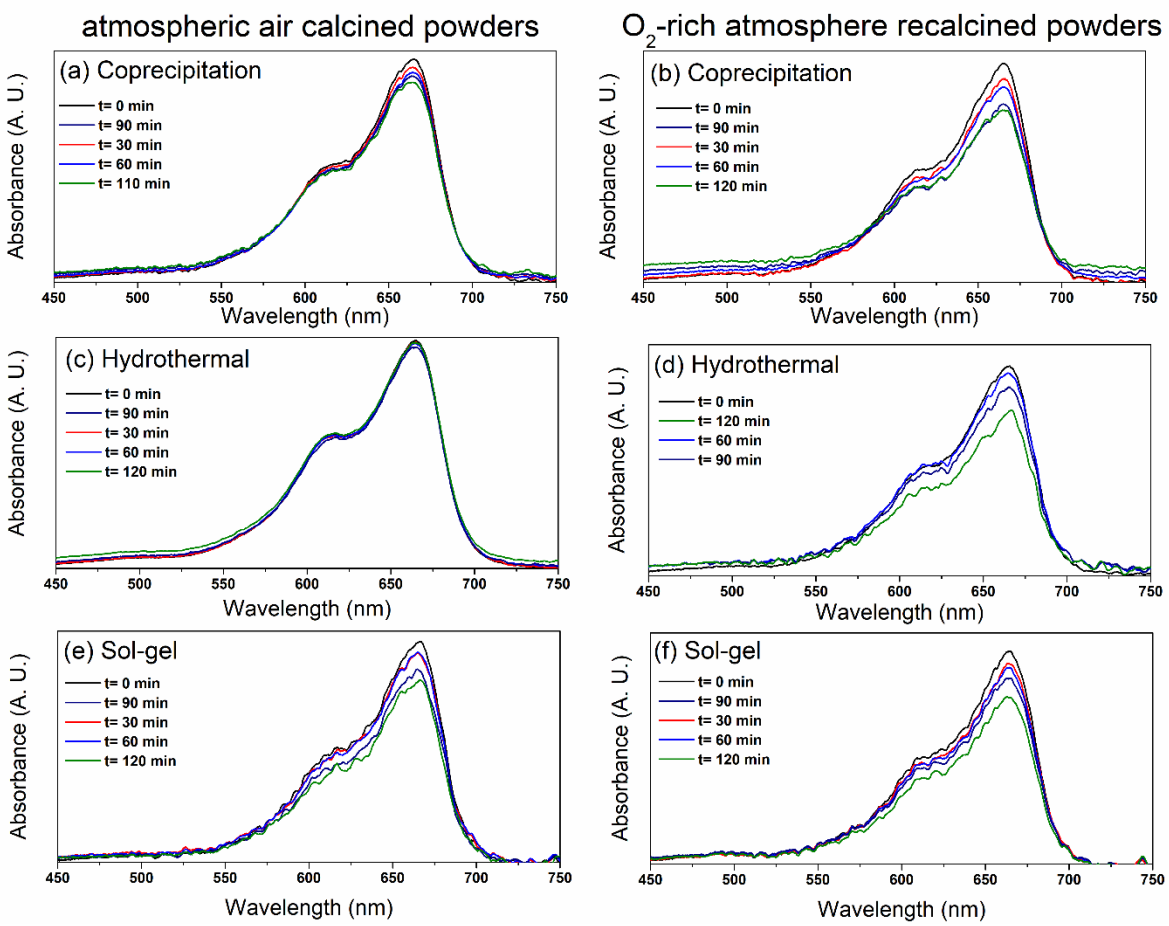

Sample	Lattice param. (Å)	Williamson-Hall method		SSP method	
		Size (nm)	microtrain (ε)	Size (nm)	Microstrain (ε)
Coprecipitation – air calcined	4.1786	60.3	-5.35 x 10^{-6}	65.4	2.01 x 10^{-3}
Coprecipitation – O_2 recalcined	4.1783	83.0	1.24 x 10^{-4}	77.9	1.67 x 10^{-3}
Hydrothermal – air calcined	4.1787	51.4	-1.74 x 10^{-4}	58.8	1.79 x 10^{-3}
Hydrothermal – O_2 recalcined	4.1788	83.0	1.52 x 10-4	72.9	1.13 x 10^{-3}
Sol gel – air calcined	4.1782(5)	83.5	1.49 x 10^{-4}	77.0	1.71 x 10^{-3}
Sol gel – O_2 recalcined	4.1782(1)	77.0	8.96 x 10^{-5}	70.7	6.36 x 10^{-4}